Enhancing Safety in Collaborative Cable-Driven Parallel Robots: Contact Distinction and Management for Carrying Tasks

Hanbang Gao, Christine Chevallereau, and Stéphane Caro

***Abstract*—Cable-Driven Parallel Robots (CDPRs) have shown significant potential in industrial applications due to their large workspace, high payload capacity, and flexibility. Nonetheless, ensuring safe and efficient human-robot collaboration, particularly during carrying tasks, remains an open problem. This paper primarily contributes a cable tension–based metric for detecting contact events, combined with a frequency-domain analysis of estimated external wrenches to distinguish different contact scenarios. Building upon this framework, three common contact scenarios are then addressed: (i) payload placement and removal without rigid attachment to the moving-platform (SC1), (ii) unintentional human-cable collisions (SC2), and (iii) human-platform collisions (SC3). Specific management strategies are then proposed, including real-time mass estimation for payload handling, cable tension release for human-cable collisions, and a compliant trajectory controller for human-platform collisions. Experimental validations on a CDPR prototype demonstrate accurate scenario classification and safe contact handling without compromising overall productivity. By facilitating safer interactions, improved adaptability, and reliable handling of diverse contact events, this work expands the applicability of collaborative CDPRs in real-world industrial and logistic settings.**

***Note to Practitioners*—In many industrial applications, robots operating alongside human workers must quickly detect and respond to contact events to maintain safety and efficiency. Traditional methods often rely on force thresholds, which can introduce delays or false alarms, especially in dynamic tasks where rapid collisions must be addressed. Our work proposes an alternative approach that utilizes a frequency-domain analysis of sensed cable tensions and a weight-score system to robustly distinguish among various contact scenarios. By examining tension signals in the frequency domain, more nuanced information can be extracted, enabling faster and more accurate responses than threshold-based methods. From a practical standpoint, this technique is relatively straightforward to implement with various sensors, and it can be adapted to robots composed of different materials and link configurations by tuning the weight-score system for each new setup. Its primary benefit is improved contact distinction with high precision, which can enhance operator safety and reduce downtime without requiring extensive hardware modifications. However, like any sensor-driven control method, performance depends on adequate calibration and consistent signal quality. Future research might focus on integrating additional sensing modalities (e.g., vision or proximity sensors) and exploring broader deployment in diverse collaborative robot systems.**

***Index Terms*—Tendon/Wire Mechanism, Parallel Robots, Human-Robot Collaboration, Physical Human-Robot Interaction, Safety in HRI.**

Manuscript received February 18, 2025; revised June 19, 2025; accepted July 6, 2025. Date of current version: July 8, 2025. This article was recommended for publication by Editor Z. Li and Editor-in-Chief Y. Sun upon evaluation of the reviewers' comments. This work was supported in part by ROBOTEX 2.0 (ANR-10-EQPX-44-01), TIRREX (ANR-21-ESRE-0015), and Titanbot (ANR-23-DMRO-0020), and was partially supported by the Agence Nationale de la Recherche under the France 2030 program, reference PEPR O2R–AS1 (ANR-22-EXOD-0005). Corresponding author: Stéphane Caro.

Nantes Université, École Centrale Nantes, CNRS, LS2N, UMR 6004, F-44000 Nantes, France. {hanbang.gao, christine.chevallereau, stephane.caro}@ls2n.fr

Digital Object Identifier (DOI):

I. Introduction

PARALLEL robots have attracted significant attention for their high precision, rigidity, and efficiency, achieved by employing multiple actuators arranged in parallel for stable and versatile motion [1]. Among these, Cable-Driven Parallel Robots (CDPRs) stand out due to their lightweight structure and relatively large workspaces, enabled by reconfigurable cable arrangements [2], [3].

CDPRs feature a high payload-to-weight ratio, large workspace, cost efficiency, and high reconfigurability [4], making them particularly useful for industrial applications such as precision manipulation tasks (e.g., machining, painting, medical procedures) [5]–[7], as well as material handling, logistics, construction, and assembly [8]. In summary, the combination of a large reachable workspace, flexible reconfiguration, and relatively simple hardware renders CDPRs ideal for tasks that span from delicate manipulation to heavy-load transport. Although collaborative CDPRs have emerged as a novel research topic to meet modern demands for flexibility and performance, only limited studies have been conducted in this area.

Specifically, collaborative CDPR presents distinct safety-critical challenges compared to traditional robots. For instance, human–cable collisions can generate contact pressures in the order of MPa due to thin cables under significant pretension, far exceeding human comfort and safety limits, thus necessitating rapid tension-release strategies [9].

In the context of Industry 4.0, collaborative robots are critical for harnessing human-robot synergy, optimizing workflows, and meeting increasing demands for flexibility and customization [10]–[12]. Collaborative CDPRs enhance system versatility and adaptability by executing tasks that involve direct human interaction, such as rehabilitation, human augmentation, and co-manipulation in industrial settings. Unlike conventional CDPRs, which are designed for predefined tasks, collaborative CDPRs can adjust to dynamic and unpredictable environments. They are often equipped with sensors and

algorithms for collision detection and avoidance, enabling safe operation around humans without the need for extensive physical barriers. Despite these benefits, collaborative CDPRs with physical Human-Robot Interaction (pHRI) introduce new challenges in intentional human-robot communication and unintentional collision management within the shared workspace. Figure 1 depicts a representative scenario in which a human operator is assisting the CDPR in carrying a payload, highlighting the integration of human effort with robotic assistance in an industrial or logistic context.

Fig. 1: Human-robot collaborative setup in which a human operator is loading a payload onto a CDPR

Human-robot collaboration has been widely studied in serial and parallel robots [13], [14], where compliance-based control strategies (e.g., impedance and admittance) relying on force sensing are regarded as effective solutions [15]. Recent work has extended these methods to collaborative CDPRs, examining, for instance, how CDPR stiffness affects transparency (the robot's ability to move in the user's intended direction) during co-manipulation [16] and proposing advanced control strategies for enhanced physical interaction [17]. Such approaches can enable co-manipulation without predefined trajectories via direct force sensor measurements. However, human operators in CDPR-based carrying tasks may interact with cables or the moving-platform (MP), not necessarily with an instrumented handle that embeds a force sensor.

Ensuring safe interaction in a CDPR that follows a predefined trajectory demands sophisticated real-time collision avoidance, detection, and management. Recent research [18] emphasizes the necessity of detecting and mitigating impacts from a fast-moving MP to ensure compliance with ISO/TS 15066 safety standards [19], which specify detailed biomechanical limits, including maximum allowable contact forces and pressures for various human body regions, to prevent injury during pHRI. Thin cables can exert significant pressure when colliding with a human [9], and the MP can reach high speed and acceleration, posing potential risks to both operator safety and system stability. Conventional CDPRs also encounter self-interference issues involving cable-cable or cable-MP interference [20], [21], along with failures in cables, motors, or encoders [22], [23]. Some studies address known obstacles by generating collision-free trajectories [24] or reconfiguring the CDPR [25], [26] for collision avoidance, while others consider geometric and dynamic effects such as cable wrapping around cylindrical surfaces [27], [28]. In unknown and human-involved environments, collision management has mainly focused on human-cable contacts, where tension measurements detect collisions and prompt cables to be released to a safer tension without altering the original trajectory [9], [29], [30]. Nevertheless, existing research has not addressed human-MP collisions with concrete experimental results, likely due to the lack of direct contact-force measurement and associated safety concerns.

Integrating safety management into collaborative CDPR frameworks remains a cutting-edge direction for industrial implementation. A general-purpose industrial motion-control architecture proposed in [31] describes a two-layer structure containing a safety controller and a motion controller, applicable to tool-path scenarios. Another approach addresses collaborative manipulation of a cable-suspended platform activated by a serial robot [32], distinguishing collisions from cooperative contacts via frequency analysis.

Previous investigations on contact distinction have primarily focused on differentiating voluntary from unintentional contacts. One family of methods is data-driven and relies on large training sets [33], whereas another applies heuristic thresholds on contact force or torque [34], [35]; both categories suffer from either heavy data requirements or sensitivity to threshold tuning. A frequency-domain perspective was introduced in [36] and refined in [37], noting that deliberate forces usually occupy lower frequency bands than collision impulses. Most recently, [32] validated frequency-based contact detection for a cable-suspended cooperative scenario, yet the study did not address human–cable collisions or their management. Likewise, the earlier works [35]–[37] rely on a single force threshold rather than a composite criterion. To the best of our knowledge, the present paper is the first to introduce a *scoring-based* method for contact distinction in CDPRs, while explicitly incorporating human–cable collisions and their management into a unified framework.

However, applying these strategies to collaborative CDPRs introduces further complexity. A critical aspect of this complexity is the possibility of contact misclassification: cooperative human efforts could mistakenly be interpreted as collisions, halting operations unnecessarily, whereas actual collisions might be overlooked due to uncertainties such as cable sag or sensor noise, as emphasised in recent studies [38]. Existing contact-distinction methods often do not differentiate human-cable from human-MP collisions, despite their distinct dynamics [32], [36], and pure admittance control without predefined trajectories rarely captures common industrial requirements for higher robot stiffness [16], [17], [39]. Industrial scenarios typically involve autonomous carrying tasks with intermittent human participation, highlighting the need for real-time intent detection and collision management to support seamless collaboration.

II. Methodological Framework

In this section, the three common contact scenarios of human-assisted CDPR carrying tasks in industrial or logistics settings are introduced to define the scope of this study. Rel-

evant assumptions are then presented. The following subsection explains the proposed management framework for these scenarios through an integrated flowchart. Lastly, the CRAFT platform and associated experimental setup are described, showing how the proposed methods are implemented.

A. Contact Scenarios in Carrying Tasks

CDPRs in industrial and logistics domains offer a large workspace and a favorable payload-to-mass ratio, making them suitable for cargo transportation. They can be integrated into flexible manufacturing systems or automated warehouses for various handling operations. Figure 1 illustrates a typical scenario: a human operator placing a box onto the MP of a CDPR. In more general industrial processes, the MP may continue following a reference trajectory while payloads are added or removed. This is referred to as Scenario Case 1 (SC1), indicating that placement and removal can occur even when the MP is not in static equilibrium.

The shared workspace between the robot and human can lead to unintentional collisions involving the operator and either the cables or the MP during operation. Human–cable contact and human–MP contact constitute Scenario Cases 2 (SC2) and 3 (SC3), respectively. These contacts are treated as unintentional collisions rather than cooperative manipulation. Minor interactions are not detected (as explained in Section IV), and once a collision is formally detected, it is managed to ensure operator safety and CDPR stability.

- **SC1: Payload Placement and Removal.** The payload is placed on top of the MP without being rigidly attached to the MP frame. It is assumed that the operator places the payload gently (with a minimum mass of approximately 500 g and a maximum of 10 kg). During payload placement, there is no direct human–MP contact, and the payload is not expected to slide on the platform. There are no further assumptions regarding payload removal beyond the absence of direct human–MP contact.
- **SC2: Human–Cable Collision.** It is assumed that only one cable is involved in a collision at any given time, as illustrated in Fig. 2. Once the collision is removed and properly managed, a subsequent human–cable collision may occur. The collided cable is assumed to lie within a Wrench Feasible Workspace (WFW) that allows tension release, effectively reducing the cable tension to zero.
- **SC3: Human–MP Collision.** This scenario considers contact between the human operator and the MP frame, typically from the side of the platform. Since the MP transports payloads primarily in a horizontal plane, a direct vertical (top-to-bottom or bottom-to-top) collision is less likely. Collisions are assumed to be instantaneous rather than gradual force applications over time, which still represent realistic industrial cases.
- **Non-Concurrent Contacts.** All three scenarios are assumed to occur sequentially rather than simultaneously. A new contact scenario is initiated only after the currently managed contact has been fully resolved. Note that payload placement and payload removal are regarded as two separate events, and both human–cable and human–MP collisions may occur after a payload has been placed.

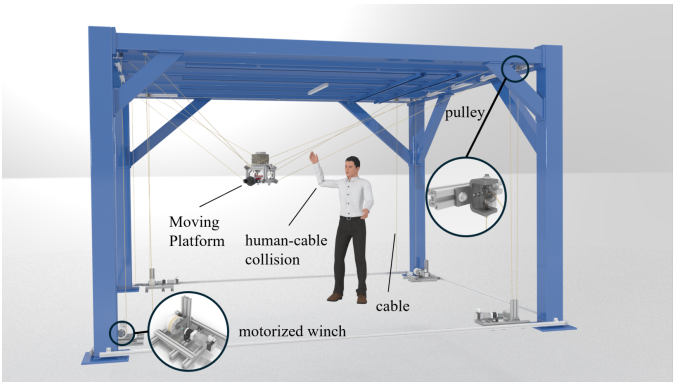

Fig. 2: A human-cable collision and the CRAFT experimental setup

Fig. 3: Scheme of human-MP collision in CDPRs

B. Proposed Framework

Figure 4 depicts the proposed workflow. After system initialization, an estimation of the payload mass is performed to update the MP's total load for inverse modeling in Cartesian-to-motor space. The CDPR executes the reference trajectory based on this dynamic information. If contact is detected via real-time monitoring using the cable tension sensors, a contact distinction procedure is initiated to determine whether SC1, SC2, or SC3 has occurred.:

- **SC1:** When a payload is placed or removed, its mass is re-estimated using the CDPR dynamic model. This estimation is performed over a period of time until the changes become negligible, and then the mass is fixed. This procedure is necessary to accurately detect and distinguish human-robot contacts.
- **SC2:** In the event of a human–cable collision, tension in the collided cable is released to a permissible level while the reference trajectory continues.
- **SC3:** For a human–MP collision, the reference trajectory is modified using a compliant controller sub-modules. The compliance sub-module interprets external forces to adjust the reference trajectory, and ensures a return to the original trajectory once the collision is resolved. The scenario ends when the modified and original trajectories converge below a predefined threshold.

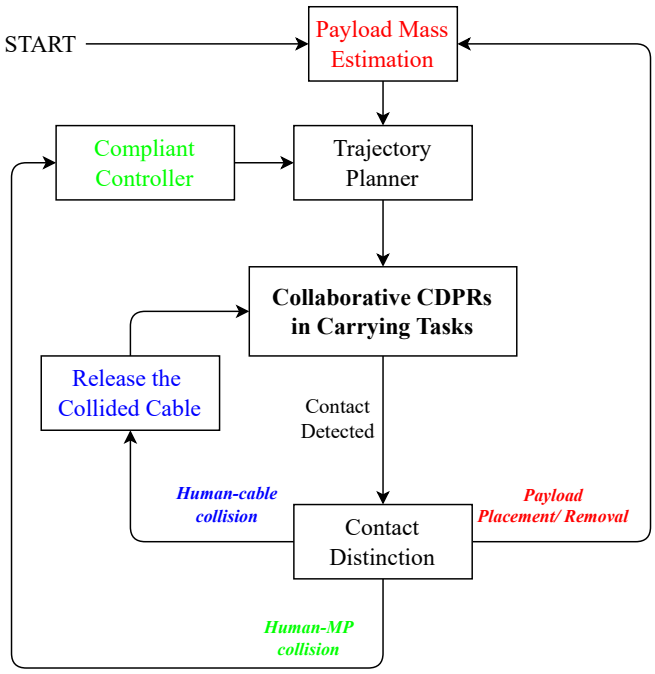

Fig. 4: Workflow of the proposed system for contact detection and management. Each box represents a task phase, while the colored text and corresponding boxes highlight the scenario detected after the contact distinction. Red corresponds to SC1, blue to SC2, and green to SC3, with each color denoting the scenario management strategy.

C. Experimental Setup

The CRAFT platform at LS2N is a CDPR prototype featuring eight suspended cables and dedicated actuation units, as shown in Fig. 2. Each actuation chain comprises a motor with an integrated gearhead, a winch, and a cable attached to the MP. The system is managed by a supervisory PC that communicates with a real-time computer (dSPACE), which regulates the torque commands for all eight motors.

Two types of sensor data are available at a sampling rate of 1 kHz:

1) **Motor Encoders:** Provide joint angles $\mathbf{q}_m$ to the real-time PC.
2) **Dynamometers:** Positioned near cable attachment points, transmitting cable tension measurements $\boldsymbol{\tau}_m$ to the real-time PC.

An embedded exponential moving average (EMA) filter processes $\boldsymbol{\tau}_m$ to yield the filtered tension $\boldsymbol{\tau}_{mf}$ [30]. The overall architecture facilitates closed-loop control and real-time monitoring, enabling the implementation of the proposed framework for contact detection, distinction, and management.

III. Robot Modeling, Control, and Trajectory Planning

In this section, the modeling of the CDPR, the control scheme corresponding to Fig. 4, and the trajectories used in the experiments are presented. The methodology includes the Inverse Geometric Elasto-static Model (IGEM), the Inverse Kinematic Model (IKM), and the dynamic model.

A. Robot Modelling

1) IGEM: The IGEM establishes a mapping between the Cartesian pose of the MP and the corresponding motor angles in the joint space. It incorporates pulley geometry [17] and linear cable elasticity [40], thereby ensuring improved accuracy in cable length computation by explicitly accounting for the dependence on the desired cable tension $\boldsymbol{\tau}_d$. Although more sophisticated nonlinear elasticity models have been studied [41], this work assumes linear elasticity behavior within the specified load range. Cable mass, which, as discussed in [20], contributes to increased sagging and reduced accuracy. Thus a light 0.7 mm-diameter cable with a mass of 4 g/m is employed, and as sagging effects are negligible for payloads exceeding 5 kg, the cable is considered massless for this study. An accurate IGEM is vital for precise Cartesian trajectory tracking of the MP.

2) IKM: For CDPRs, the forward Jacobian matrix is equals to $-\mathbf{W}^\top$, which transforms the platform velocity in Cartesian coordinates, $\mathbf{v}$, into the cable unwinding velocities $\dot{\mathbf{l}}$:

$$-\mathbf{W}^\top \mathbf{v} = \dot{\mathbf{l}}, \quad \text{with} \quad \mathbf{v} = \begin{bmatrix} \dot{\mathbf{p}} \\ \boldsymbol{\omega} \end{bmatrix}, \tag{1}$$

where $\mathbf{p}$ and $\dot{\mathbf{p}}$ is the Cartesian position and velocity of the MP, $\boldsymbol{\omega}$ is the angular velocity of the MP expressed in the base frame, and $\mathbf{l}$ is the vector of cable lengths from anchor positions to pulley exit points. The matrix $\mathbf{W}$, referred to as the wrench matrix.

3) Dynamic Modeling: Following [42], the dynamic model of a CDPR is

$$\mathbf{W}\boldsymbol{\tau} - \mathbb{I}_p \dot{\mathbf{v}} - \mathbf{C}\mathbf{v} + \mathbf{w}_e + \mathbf{w}_g = 0, \tag{2}$$

where $\boldsymbol{\tau}$ is the vector of cable tensions, $\mathbb{I}_p$ is the spatial inertia of the platform, and $\mathbf{C}$ is the matrix of centrifugal and Coriolis wrenches. The term $\mathbf{w}_e$ represents external wrenches (e.g., collisions and contacts), and $\mathbf{w}_g$ is the gravitational wrench. The gravity wrench $\mathbf{w}_g$ due to gravity vector $\mathbf{g} = [0, 0, -g]^\top$ is

$$\mathbf{w}_g = \begin{bmatrix} m\mathbf{I}_3 \\ \hat{\mathbf{M}}\mathbf{S}_p \end{bmatrix} \mathbf{g}, \tag{3}$$

where m is the platform mass, $g = 9.81\,\mathrm{m\,s^{-2}}$, and $\mathbf{I}_3$ denotes the 3×3 identity matrix in $\mathbb{R}^3$. The first momentum of the moving-platform with respect to the MP frame is represented by $\mathbf{M}\mathbf{S}_p$, and its corresponding skew-symmetric matrix is denoted by $\hat{\mathbf{M}}\mathbf{S}_p$. Note that the geometric center and the center of gravity of the MP do not coincide, resulting in nonzero first moments. The spatial inertia $\mathbb{I}_p$ is defined as

$$\mathbb{I}_p = \begin{bmatrix} m\mathbf{I}_3 & -\hat{\mathbf{M}}\mathbf{S}_p \\ \hat{\mathbf{M}}\mathbf{S}_p & \mathbf{I}_p \end{bmatrix}, \tag{4}$$

where the off-diagonal terms account for the first moments arising from the discrepancy between the geometric center and the center of gravity, and $\mathbf{I}_p$ is the inertia tensor of the

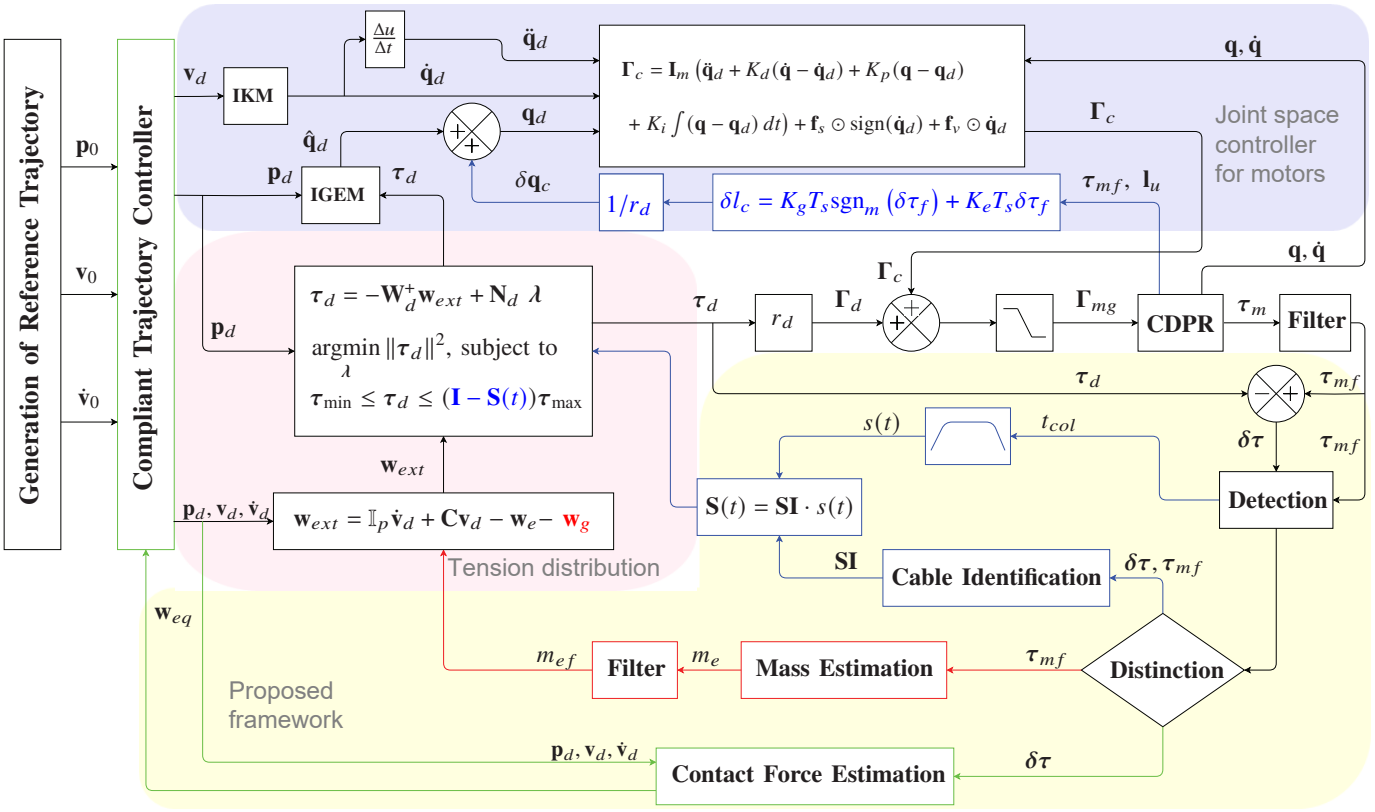

Fig. 5: Proposed control scheme of the CRAFT platform. Black blocks indicate the standard controller for nominal robot operations. Each scenario case (SC1 in red, SC2 in blue, and SC3 in green) is managed by a distinct strategy following contact detection and is activated only when the corresponding event is distinguished.

platform. It can be derived from the inertia tensor $\mathbf{I}_g$ in the MP frame using the Huygens–Steiner theorem:

$$\mathbf{I}_p = \mathbf{R}_p \mathbf{I}_g \mathbf{R}_p^T - \frac{\hat{\mathbf{M}}\mathbf{S}_p \hat{\mathbf{M}}\mathbf{S}_p}{m}. \tag{5}$$

In (2), the matrix $\mathbf{C}$ yields centrifugal and Coriolis wrenches:

$$\mathbf{C}\mathbf{v} = \begin{bmatrix} \hat{\boldsymbol{\omega}}\hat{\boldsymbol{\omega}}\mathbf{M}\mathbf{S}_p \\ \hat{\boldsymbol{\omega}}\mathbf{I}_p\boldsymbol{\omega} \end{bmatrix}, \tag{6}$$

where $\hat{\boldsymbol{\omega}}$ is the skew-symmetric matrix of $\boldsymbol{\omega}$. This formulation underpins the control design and analysis for human-assisted operations.

B. Control Architecture

Figure 5 summarizes the proposed control scheme for the CRAFT platform. Three main parts, highlighted in colored patches, constitute the architecture:

- **Purple (Joint Space Controller):** Implements a computed torque control law with PID correction, driving motors from measured angles $\mathbf{q}$ to desired angles $\mathbf{q}_d$. Desired values $\mathbf{q}_d$ are computed via the IGEM, enabling accurate tracking in joint space.
- **Pink (Tension Space Controller):** Translates desired motion commands of the MP into desired cable tensions $\boldsymbol{\tau}_d$. A feed-forward term $\mathbf{w}_{ext}$ derived from the inverse dynamic model compensates for inertia, Coriolis, and gravitational effects.
- **Yellow (Proposed System for Contact Distinction and Management):** Monitors sensor signals in real time, identifies collisions, and applies the appropriate strategy (SC1, SC2, or SC3) based on the contact distinction framework.

Black blocks within Fig. 5 represent components dedicated to nominal operation, including the motor-gearbox torque $\boldsymbol{\Gamma}_{mg}$. A saturation function ensures safe operating limits. The joint space controller outputs $\boldsymbol{\Gamma}_c$ after accounting for frictional effects and desired accelerations, while the tension space controller generates $\boldsymbol{\Gamma}_d$ to regulate cable tensions. The combination of $\boldsymbol{\Gamma}_c$ and $\boldsymbol{\Gamma}_d$ forms the total command $\boldsymbol{\Gamma}_{mg}$.

1) Joint Space Controller: The desired motor angles $\mathbf{q}_d$ are computed via the IGEM, and a PID corrector with gains K_p^q, K_i^q, and K_d^q forces the tracking error $\mathbf{e}_q = \mathbf{q} - \mathbf{q}_d$ to converge to zero:

$$\ddot{\mathbf{e}}_q + K_d\,\dot{\mathbf{e}}_q + K_p\,\mathbf{e}_q + K_i \int \mathbf{e}_q\,dt = 0. \tag{7}$$

The motor joint acceleration is defined as:

$$\ddot{\mathbf{q}} = \ddot{\mathbf{q}}_d - K_d\,(\dot{\mathbf{q}} - \dot{\mathbf{q}}_\mathbf{d}) - K_p\,(\mathbf{q} - \mathbf{q}_d) - K_i \int (\mathbf{q} - \mathbf{q}_d)\,dt. \tag{8}$$

Coulomb and viscous friction are compensated by

$$\boldsymbol{\Gamma}_c = \mathbf{I}_m \ddot{\mathbf{q}} + \mathbf{f}_s \odot \operatorname{sign}(\dot{\mathbf{q}}_d) + \mathbf{f}_v \odot \dot{\mathbf{q}}_d, \tag{9}$$

where $\mathbf{I}_m$ is the inertia matrix of the motor–gearbox and $\odot$ represents element-wise multiplication. $\mathbf{f}_s$ is the static friction and $\mathbf{f}_v$ is the viscous friction.

2) Tension Space Controller: To ensure desired motion, the motor torques $\mathbf{\Gamma}_d$ are computed by determining the cable tensions $\boldsymbol{\tau}_d$. A feed-forward term $\mathbf{w}_{ext}$ from the (2) compensates for the system dynamics:

$$\mathbf{w}_{ext} = \mathbb{I}_p \dot{\mathbf{v}}_d + \mathbf{C}\mathbf{v}_d - \mathbf{w}_e - \mathbf{w}_g, \tag{10}$$

where $\mathbf{v}_d$ is the desired platform velocity. The tensions $\boldsymbol{\tau}_d$ are optimized using quadratic programming [29]:

$$\min_{\boldsymbol{\lambda}} \|\boldsymbol{\tau}_d\|^2, \quad \text{subject to} \quad \boldsymbol{\tau}_{\min} \le \boldsymbol{\tau}_d \le \boldsymbol{\tau}_{\max}, \tag{11}$$

where $\boldsymbol{\lambda}$ is a two-dimensional vector representing the null space variables. The selection of $\boldsymbol{\lambda}$ is critical for optimizing the norm of the tensions. The vector $\boldsymbol{\tau}_{\min}$ ensures cable tautness by maintaining a minimum tension of 1 N per cable, while $\boldsymbol{\tau}_{\max}$ sets the upper limit at 100 N per cable.

The tension vector $\boldsymbol{\tau}_d$ is defined as

$$\boldsymbol{\tau}_d = -\mathbf{W}_d^{+}\mathbf{w}_{ext} + \mathbf{N}_d\boldsymbol{\lambda}, \tag{12}$$

where $(\cdot)^{+}$ denotes the Moore–Penrose pseudo-inverse, and $\mathbf{W}_d$ is the desired wrench matrix derived from the IGEM, and $\mathbf{N}_d$ is the null space of $\mathbf{W}_d$, satisfying $\mathbf{W}_d\mathbf{N}_d\boldsymbol{\lambda} = \mathbf{0}_6$. The position of the MP is calculated using the IGEM, which ensures accurate trajectory tracking by accounting for the geometric constraints of the system. The resulting motor–gearbox torque is given by

$$\mathbf{\Gamma}_{mg} = \text{sat}(r_d\,\boldsymbol{\tau}_d + \mathbf{\Gamma}_c), \tag{13}$$

where $\text{sat}(\cdot)$ denotes a saturation function that ensures the output torque of the motors remains within acceptable limits, and r_d represents the winch radius.

C. Trajectory Design

Two trajectories were designed to evaluate system performance:

1) Static Trajectory: The MP remains stationary above the test stand with active servo motors. This setup assesses contact detection and distinction under quasi-static conditions.

2) Dynamic Trajectory: The MP moves along a 1 m square planar path over 60 s at an average speed of 0.1 m/s. A fifth-order polynomial trajectory governs position, velocity, and acceleration, ensuring smooth transitions and effective contact management during dynamic interactions. Each segment uses a quintic polynomial of the form:

$$\mathbf{p}(t) = \mathbf{p}_0 + (\mathbf{p}_f - \mathbf{p}_0)\left(10\alpha^3 - 15\alpha^4 + 6\alpha^5\right), \quad \alpha = \frac{t}{T} \in [0,1],$$

where $\mathbf{p}_0$ and $\mathbf{p}_f$ are the initial and final position vectors over the segment duration T. This construction enforces zero velocity and acceleration at the start and end of each segment, resulting in smooth, continuous motion profiles that minimise mechanical stress and avoid abrupt changes in cable tension.

Note that the chosen speed and path length account for the CRAFT prototype's smaller scale compared to industrial CDPRs (with frames exceeding 20 m). Both length and velocity have been scaled to match the platform's capabilities, avoiding excessive motor loads and cable displacements. Although small-scale CDPRs can achieve higher speeds, this reduced velocity ensures safe and controlled dynamic behavior under the prototype's inherent mechanical constraints, while still demonstrating that the system dynamics extend beyond quasi-static conditions.

IV. Contact Detection

A. Overview of Contact Detection

A heuristic method for human–cable collision (SC2) detection was introduced in [29] by continuously monitoring cable tension errors. Although originally focused on SC2, this approach can be generalized to detect all three contact scenarios (SC1, SC2, and SC3). The main idea is summarized below.

B. Tension Error Metric

Define the tension tracking error $\boldsymbol{\delta\tau}$ as an eight-dimensional vector representing the difference between the measured and desired cable tensions, as illustrated by the **Detection** block in Fig. 5:

$$\boldsymbol{\delta\tau} = \boldsymbol{\tau}_{mf} - \boldsymbol{\tau}_d, \tag{14}$$

where $\boldsymbol{\tau}_{mf}$ is the measured cable tension filtered by an EMA, and $\boldsymbol{\tau}_d$ is the desired tension vector. Under normal operation (i.e., when the MP follows its reference trajectory without human interaction), the errors typically remain within 3 N. However, a threshold of 5 N is chosen empirically:

$$T_h = 5\,\text{N}, \tag{15}$$

Theoretically, this threshold can be interpreted as an upper bound derived from the combination of the system's nominal tracking noise (assumed bounded), plus a safety margin. That is:

$$T_h = \delta_{\max} + \Delta_s, \tag{16}$$

where $\delta_{\max} \approx 3\,\text{N}$ is the maximum observed tension error under nominal conditions that includes sensor noise and model-fit residuals. The margin $\Delta_s = 2\,\text{N}$ is a conservatively chosen to ensure reliable collision detection, which eliminates false positives at the cost of a predictable detection delay.

This formulation balances two objectives: (i) ensuring that minor disturbances and noise do not lead to false alarms, and (ii) capturing contact events that meaningfully alter the tension profile. The threshold is thus obtained from the observed system behaviour, consistent with practical approaches in CDPR safety studies (e.g., [31]).

C. Detection Criterion

A contact is declared if any component $\delta\tau_i$ of $\boldsymbol{\delta\tau}$ exceeds the threshold T_h:

$$\exists\, \delta\tau_i \in \boldsymbol{\delta\tau} : \delta\tau_i > T_h. \tag{17}$$

For SC2, following payload removal, the cable tensions decrease. In contrast, as analyzed in [31], placing an object

onto the platform typically involves a fast impact, whereas payload removal is generally a more gradual process. A lower threshold for payload removal is defined as $T_h^- = -4$ N. Consequently, a payload removal (SC1) is declared if any component $\delta\tau_i$ of $\boldsymbol{\delta\tau}$ falls below T_h^-:

$$\exists\, \delta\tau_i \in \boldsymbol{\delta\tau} : \delta\tau_i < T_h^-. \tag{18}$$

D. Experimental Illustration

Figure 6 shows an experiment designed to demonstrate contact detection and distinction in a stationary CDPR. The sequence includes two payload placement events and two payload removal events (SC1), two human–cable collisions (SC2), and two human–MP collisions (SC3). Each scenario is repeated twice to illustrate the generality of the proposed approach.

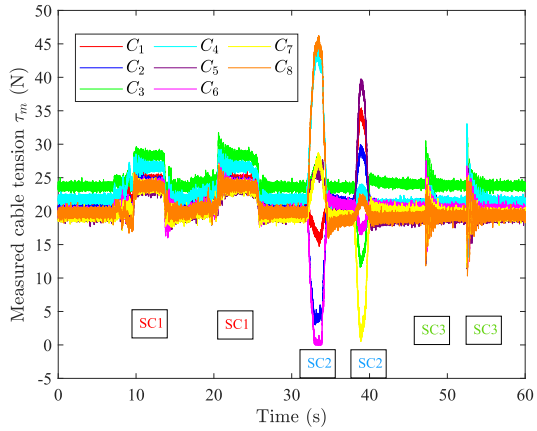

(a) Measured cable tensions

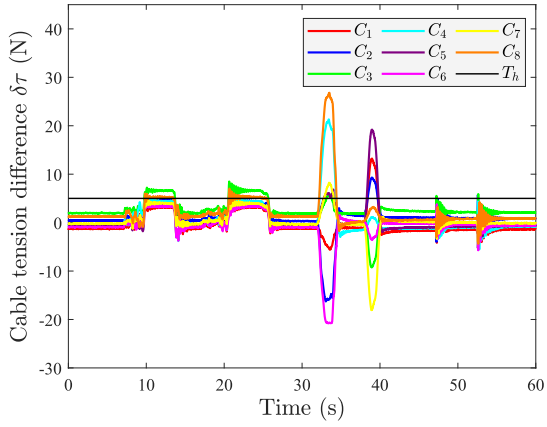

(b) Cable tension difference and the threshold T_h for detection

Fig. 6: Measured cable tension $\boldsymbol{\tau}_m$ and cable tension difference $\delta\boldsymbol{\tau}$ during a series of contact events with the CDPR in a stationary configuration. The label C_j denotes the j^{th} cable ($j = 1, 2, \ldots, 8$). T_h is the threshold for contact detection.

From the experimental results, three key observations arise:

- **SC1 (Payload Placement/Removal):** During placement, tension in all cables increases; it decreases when the payload is removed. The placement/removal act introduces small, transient oscillations.
- **SC2 (Human–Cable Collision):** Some cable tensions (including the collided cable) increase significantly, while others may drop or sag. Due to the relatively low stiffness of the cable, oscillations remain very limited because external forces are largely absorbed.
- **SC3 (Human–MP Collision):** All cable tensions show more pronounced oscillations, which gradually damp out over time as the controller regulates for the disturbance.

V. Contact Distinction

In collaborative CDPR carrying tasks, accurately distinguishing among different types of contact events is vital for ensuring both operator safety and system robustness. In this section, we propose a real-time contact-distinction framework consisting of: (i) estimation of the external wrench acting on the moving-platform, (ii) extraction of spectral norm derivative (SND) indices via frequency-domain analysis, and (iii) a deterministic scoring-based classifier that assigns each event to one of three scenarios.

A. Methodology

Based on the dynamic model in (2), the external wrench $\mathbf{w}_{eq}$ exerted on the MP can be estimated as:

$$\mathbf{W}_d\boldsymbol{\tau}_{mf} - \mathbb{I}_p\dot{\mathbf{v}}_d - \mathbf{C}\mathbf{v}_d + \mathbf{w}_{eq} + \mathbf{w}_g = 0, \tag{19}$$

where $\boldsymbol{\tau}_{mf}$ is the measured filtered cable tension, $\mathbf{W}_d$ is the desired wrench matrix, $\mathbb{I}_p$ is the platform's spatial inertia, $\mathbf{C}$ is the matrix of Coriolis and centrifugal wrenches, and $\mathbf{w}_g$ is the gravitational wrench. The term $\mathbf{w}_{eq}$ is a rough estimate of the equivalent external wrench to be determined, i.e.,

$$\mathbf{w}_{eq} = \begin{bmatrix} f^x & f^y & f^z & m^x & m^y & m^z \end{bmatrix}^\top, \tag{20}$$

where f^i and m^i denote the forces and moments along each axis i, respectively. Note that for human–cable collisions, the dominant external effect is the force component. Although cable tensions can generate a moment about the geometric center of the MP, this moment is usually negligible compared to the forces.

1) Frequency-Analysis: To differentiate these scenarios more reliably, a frequency-based criterion is applied rather than relying solely on force thresholds [37]. At each time instant, a Fast Fourier Transform (FFT) is computed over a sliding window of N samples of the raw force signal $\mathbf{f}_{\text{eq}}$ (specifically, the first three elements of the estimated wrench $\mathbf{w}_{\text{eq}}$ in (19)), weighted by a half-Hann window w. Denoting f^j as the j-th component of $\mathbf{f}_{\text{eq}}$ (with $j = x, y, z$), its FFT is represented as $F^j(n)$, and the magnitude $F^j_\omega(m)$ of the discrete Fourier transform is computed as

$$F^j_\omega(m) = \left\| \sum_{n=0}^{N-1} w_n\, F^j(n)\, e^{-2\pi i\, \frac{m\,n}{N}} \right\|, \quad m = 0, \ldots, N-1, \tag{21}$$

where the half-Hann window is defined as

$$w_n = \frac{1}{2}\left(1 - \cos\left(\frac{2\pi n}{2N-1}\right)\right), \quad n = 0, \ldots, N-1. \tag{22}$$

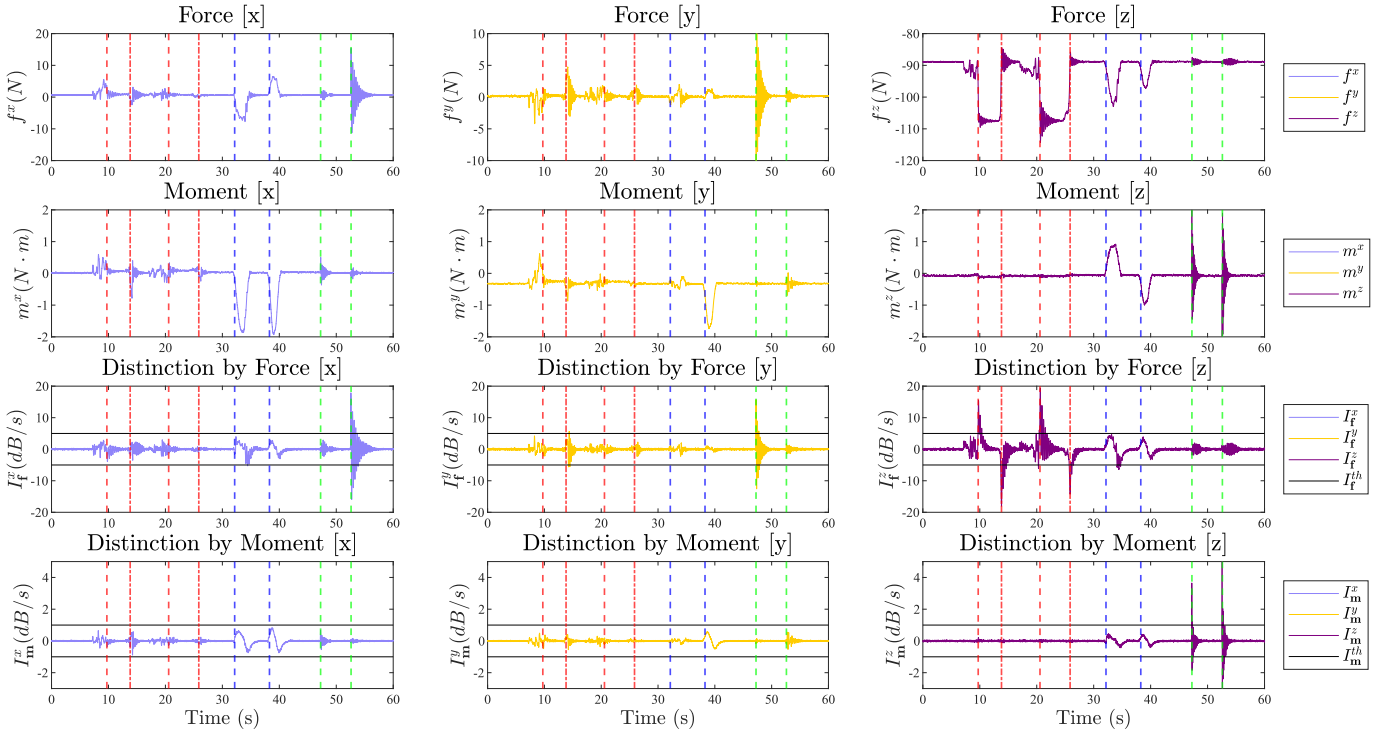

Fig. 7: Static Experiment: The top two rows display the estimated external forces and moments acting on the MP. The third and bottom rows show the spectral norm derivative (SND) indices for forces and moments along the x, y, and z axes. Colored vertical lines indicate detected contacts: red for SC1, blue for SC2, and green for SC3. The red dashed line indicates the payload placement, while the red dash-dotted line indicates the payload removal. Black lines in the third and fourth rows represent the proposed SND index thresholds for forces and moments, respectively.

This window function assigns higher importance to recent measurements while progressively de-emphasizing older data. The window length N is chosen based on the desired frequency resolution $\Delta\omega = \frac{1}{T_s N}$, where T_s is the sampling period. Frequencies below $\omega_{\min}$ are associated with slower, voluntary interactions, while frequencies above $\omega_{\max}$ are assumed to be sensor noise.

To capture meaningful collision-related dynamics, the analysis focuses on the frequency band $[\omega_{\min}, \omega_{\max}]$. The Spectral Norm Derivative (SND) index for the j-th component, $I_{\mathbf{f}}^{j}$, is defined as:

$$I_{\mathbf{f}}^{j} = \frac{d}{dt}\left\|\mathbf{F}^{j}_{[\omega_{\min},\,\omega_{\max}]}\right\|_1, \tag{23}$$

where $\mathbf{F}^{j}_{[\omega_{\min},\,\omega_{\max}]}$ represents the sub-vector of frequency components within the chosen range, and $\|\cdot\|_1$ denotes the ℓ_1-norm (i.e., the sum of the magnitudes of these components). Regarding the use of the ℓ_1-norm on the magnitude spectrum, this choice improves robustness to narrow-band spectral peaks (e.g., resonances) and offers a linear, interpretable metric whose time derivative reflects the net change in frequency content. These properties are desirable for reliable contact distinction in noisy environments. Hence, $I_{\mathbf{f}}^{j}$ captures the rate of change in the frequency content for the j-th axis. Similarly, $I_{\mathbf{m}}^{j}$ is obtained by applying the same procedure to the moment vector $\mathbf{m}_{\text{eq}} = [m^x, m^y, m^z]$ of the estimated wrench.

In this study, $\omega_{\min} = 3\,\text{Hz}$ is selected to exclude typical low-frequency motion of the MP (which is not related to collisions), and $\omega_{\max} = 50\,\text{Hz}$ is used to include human–robot interaction frequencies while omitting high-frequency noise. The sampling period is set to $T_s = 0.001\,\text{s}$, and $N = 1024$ yields a window of $1.024\,\text{s}$. Thus, each SND index estimate leverages the most recent $1.024\,\text{s}$ of wrench data, ensuring that significant transient events can be distinguished promptly.

2) Distinction Criteria: From the observations of SC1, SC2, and SC3, the SND indices for both force and moment components along the x, y, and z axes can be used to distinguish contact. Figure 7 illustrates the estimated external forces and corresponding SND indices for the static experiment described in Section IV. The figure is organized into four rows: the first row displays the force components, the second row shows the moment components, the third row presents the SND indices for forces, and the fourth row presents the SND indices for moments. Each column corresponds to one of the Cartesian axes $(x,\, y,\, z)$.

- **SC1 (Payload Placement/Removal):** When a payload is placed or removed, the force along the z-axis increases or decreases substantially, accompanied by minor transient oscillations. In most trials, in-plane components (x and y) remain low, although diagonal placement may induce more noticeable in-plane forces. Consequently, $I_{\mathbf{f}}^{z}$ tends to be larger, while $I_{\mathbf{f}}^{x,y}$ are relatively small. Because the predominant force is parallel to the z-axis, $I_{\mathbf{m}}^{z}$ also remains small; similarly, $I_{\mathbf{m}}^{x,y}$ are generally small when the payload is placed gently.

- **SC2 (Human–Cable Collision):** The forces evolve more gradually across all axes rather than showing abrupt changes. This behavior arises from the cable damping, which dissipates a portion of the external interaction force. Consequently, SC2 exhibits relatively small SND indices for both forces and moments.
- **SC3 (Human–MP Collision):** Transient oscillations appear in all axes when a collision occurs, although the amplitude in the z-axis is usually smaller, consistent with the assumption that vertical collisions are less frequent. Such interactions often yield larger SND indices for forces and moments along the x or y axis (or both). However, the amplitude distribution of these indices depends on the collision type and impact location; the maximum indices may not always occur along the x or y axes exclusively. Additionally, an abrupt rotational interaction may produce a high $I_{\mathbf{m}}^{z}$.

Based on these findings, Table I introduces a scoring-based framework for distinguishing contact scenarios. Each row corresponds to a scenario (SC1, SC2, SC3), and each column represents a condition checked against a chosen threshold. The table employs a "true" (✓) and "false" (✗) notation to indicate whether a specific force or moment criterion is exceeded. Weighted scores are assigned or subtracted based on the relevance of each condition: green cells indicate a score of 1 for high relevance, yellow cells represent a score of 0.5, and grey cells denote a score of 0.25 for partial relevance, depending on whether the condition is satisfied. After evaluating all conditions, the scenario with the highest cumulative score is declared the contact type. Furthermore, to ensure a fair comparison across scenarios, the cumulative scores are bounded between 0 and 1, where 1 corresponds to the highest relevance and 0 indicates no relevance. This method avoids ambiguity from overlapping criteria or the limitations of a single threshold. This is especially useful when multiple contact types exceed the threshold simultaneously, enhancing discrimination accuracy.

TABLE I: Scoring-Based Classification of Contact Events. Cells show the threshold outcome (✓/✗) and, by background color, the weight assigned to that condition: ■ 1.0, ■ 0.5, ■ 0.25. The scenario with the highest total weight is selected.

Scenario	$I_{\mathbf{f}}^{x,y} > I_{\mathbf{f}}^{th}$	$I_{\mathbf{f}}^{z} > I_{\mathbf{f}}^{th}$	$I_{\mathbf{m}}^{x,y} > I_{\mathbf{m}}^{th}$	$I_{\mathbf{m}}^{z} > I_{\mathbf{m}}^{th}$
SC1	✗	✓	✗	✗
SC2	✗	✗	✗	✗
SC3	✓	✗	✓	✓

B. Results and Discussion

The threshold values for the SND indices are empirically determined: $I_{\mathbf{f}}^{th} = 5\,\text{dB/s}$ for force and $I_{\mathbf{m}}^{th} = 1\,\text{dB/s}$ for moment components. These thresholds are selected based on multiple contact experiments under varying tasks.

In the static experiment, by combining Fig. 6 and the SND index outcomes in Fig. 7, the following distinction results are obtained. Table II summarizes eight sequentially detected contact events. For instance, "Exp. j" denotes the j^{th} contact event detected during the experiment; Exp. j^{+} indicates a mass placement, while Exp. j^{-} corresponds to a mass removal. Each row lists the computed scores for SC1, SC2, and SC3, followed by the final distinction results. The results show that the predicted contact scenario matches the actual contact in each trial.

TABLE II: Classification Results for Static Experiments

Experiments	Normalized Scores			Results
	SC1	SC2	SC3	
Exp.1^{+}✗✓✗✗	1.00	0.75	0.00	SC1
Exp.1^{-}✓✓✗✗	0.90	0.50	0.18	SC1
Exp.2^{+}✗✓✗✗	1.00	0.75	0.00	SC1
Exp.2^{-}✗✓✗✗	1.00	0.75	0.00	SC1
Exp. 3 ✗✗✗✗	0.60	1.00	0.36	SC2
Exp. 4 ✗✗✗✗	0.60	1.00	0.36	SC2
Exp. 5 ✓✗✗✓	0.10	0.50	0.81	SC3
Exp. 6 ✓✗✗✓	0.10	0.50	0.81	SC3

Additional trials (320 in total) were conducted under both static and dynamic conditions. In addition to the authors, four independent researchers with no prior knowledge of the classification algorithm executed the experiments, ensuring an unbiased assessment of the method. They were free to interact autonomously with the CDPR. Specifically, in SC1 scenario, they were permitted to either place (SC1+) or remove (SC1–) payload masses ranging from 1 to 3.5 kg, and to make contact with any of the eight cables. In SC3 scenarios, participants were instructed to knock or hit the moving-platform using a wooden cylinder, a plastic hammer, or any part of their body. Prior to the experiments, all participants received a safety briefing. During the trials, a researcher was always on standby to activate the emergency stop button if necessary.

The classification results presented in Table III demonstrate high reliability, with only 9 classification failures out of 320 trials. Notably, one failure occurred when a participant exerted excessive force on the cable (SC2), leading to cable breakage. Consequently, the saturation of control motor torque did trigger the platform built-in emergency stop and halted data logging, so no classification output was produced. Three additional failures involved minor force applied during SC3, resulting in undetected contacts due to the increment in cable tension not surpassing the threshold T_h. However, this is not critical since these collisions pose no risk to either the operator or the platform, given the low interaction forces involved. A recurring misclassification arose in five trials where participants pulled a cable sharply downward; in these cases, the rapid vertical force change was incorrectly classified as SC1+ (placement of a mass payload). This specific scenario was not initially considered in the assumptions but is practically rare in real industrial or logistical contexts, indicating that such misclassifications could be naturally avoided in typical operational scenarios.

A trade-off exists between detection responsiveness and

TABLE III: Classification Results of Contact Events

Trails	Classified as				
	SC1+	SC1-	SC2	SC3	No Contacts
SC1+	100%	0%	0%	0%	0%
SC1-	0%	100%	0%	0%	0%
SC2	5.56%	0%	93.33%	0%	1.11%
SC3	100%	0%	0%	96.66%	3.33%

contact distinction accuracy. By selecting an appropriate detection margin, Δ_s, the system effectively prevented false alarms (contact detections in the absence of actual contacts), but this introduced a detection delay ranging from approximately 150 to 500 ms, contingent on the magnitude of the applied force. The implementation of an EMA filter on cable tensions introduced a latency of around 100 to 150 ms for tension errors to reach the threshold of 5 N. Nevertheless, the overall system, operating at 1000 Hz with a 1 ms state update interval, demonstrated the capability to promptly detect and distinguish contact types significantly earlier than any substantial threat could manifest.

For context, the proposed frequency-domain contact analysis requires only 20 ms after contact detection to distinguish the event, whereas a pure force-threshold method [9], [32] must accumulate 100–250 ms of data to separate SC2 from SC3 with $\geq$ 90% accuracy under the same operating conditions. Thus the frequency-based approach provides earlier situational awareness without sacrificing reliability. These extensive tests, incorporating variable payloads, diverse force magnitudes during human–cable collisions, and multi-directional human–MP collisions, confirmed the robustness and reliability of the proposed classification method in realistic settings.

VI. Contact Management

In Subsection II-B, a workflow for managing contact scenarios while carrying tasks was introduced. Once a contact is detected and its scenario (SC1, SC2, or SC3) identified, specific actions are taken: payload mass estimation during placement (SC1), releasing the collided cable (SC2), or modifying the trajectory (SC3). While Section V presented static experimental results without the full management framework shown in Fig. 5, this section details the management processes and the criteria used to conclude each phase based on comprehensive experiments. In a 60-second dynamic trajectory, a 1.00 kg dumbbell is placed on the MP, followed by a human–cable collision, a human–MP collision, and finally, the dumbbell is removed. This experiment, which integrates all three scenarios—SC1 (payload placement and removal), SC2, and SC3—reflects real industrial and logistics applications and also safety concerns. The supplementary video and accompanying data, demonstrating the full carrying task experiment, are available[1].

[1]The supplementary video of this paper can be accessed at https://youtu.be/TDfgs-YXAOQ.

A. SC1: Payload Placement/Removal

Referring to Fig. 5, the red blocks and text denote the additional components necessary for implementing these modifications in the overall control scheme. In case a payload is placed on the MP without slipping, the overall suspended mass increases accordingly. If this increased mass is not accounted for, two primary issues arise:

- The IGEM becomes inaccurate, leading to elevated position tracking errors.
- The dynamic wrench in (10) is miscalculated, causing high tension tracking errors. These tension errors also serve as a general contact detection indicator; hence, unadjusted mass estimation would lead to persistent false contact signals.

To address these issues, the effective total mass of the MP and payload, denoted m_e, is estimated by modifying (2):

$$\mathbf{W}_d\boldsymbol{\tau}_{mf} - \mathbb{I}_p\dot{\mathbf{v}}_d - \mathbf{C}\mathbf{v}_d + \mathbf{w}_g^e = 0, \tag{24}$$

where $\mathbf{w}_g^e$ is the estimated gravitational wrench defined as

$$\mathbf{w}_g^e = \begin{bmatrix} m_e\mathbf{I}_3 \\ \hat{\mathbf{M}}\mathbf{S}_p^e \end{bmatrix}\mathbf{g}. \tag{25}$$

Here, $\mathbf{MS}_p^e$ represents the new estimated first moment of inertia for the system. In practice, the MP rarely rotates about the x or y axes during carrying tasks, rendering the variations in the first moment of inertia negligible, i.e., $\mathbf{MS}_p^e \approx \mathbf{MS}_p$. This simplification allows us to estimate m_e by solving

$$\underset{m_e}{\operatorname{argmin}} \left\| \mathbf{W}_d\boldsymbol{\tau}_{mf} - \mathbb{I}_p\dot{\mathbf{v}}_d - \mathbf{C}\mathbf{v}_d + \mathbf{w}_g^e \right\|^2. \tag{26}$$

To prevent abrupt changes from immediately affecting the IGEM, an EMA filter with smoothing factor $\alpha = 0.01$ is applied:

$$m_{ef}(t) = \alpha\, m_{ef}(t) + \big(1-\alpha\big)\, m_{ef}(t-1). \tag{27}$$

Figure 8 illustrates an example in which a 1.00 kg payload is added to a 9.05 kg MP while it follows a reference trajectory. The blue curve indicates the actual total mass, and the red curve represents the filtered estimate. Although the estimation exhibits an initial overshoot, upon reaching steady state, the estimation error remains below 0.01 kg, demonstrating the effectiveness of this mass management approach.

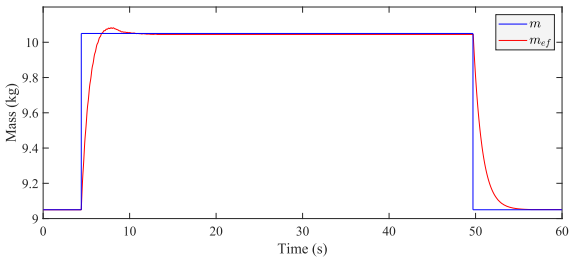

Fig. 8: Estimated filtered mass of the MP during payload placement and removal

1) Management of Payload Placement/Removal: Collisions involving the cable and the MP affect both $\mathbf{W}_d$ and $\boldsymbol{\tau}_{mf}$,

which in turn compromise the accuracy of the mass estimation provided by (26). To mitigate this issue, mass estimation is performed only briefly upon detection of payload placement/removal rather than continuously during the entire carrying task. Once SC1 is detected, the system monitors whether the effective mass m_{ef} remains within $0.005\,\mathrm{kg}$ for at least one second. When this stability criterion is met, the current estimate is maintained until the next SC1 is detected.

2) Re-calibration of Payload Mass: Upon activation of the special function, payload removal detection initiates a smooth exponential reversion of the estimated mass to the pre-measured MP mass.

B. SC2: Human–Cable Collision

Referring to Fig. 5, the blue blocks and text highlight the additional components required to manage the human-cable collision through releasing the collided cable. The method proposed in [29] is extended here, and the primary steps are summarized below:

- **Collision Detection and Cable Identification:** A collision time t_{col} is detected, and the specific cable c involved is identified [29]. The red detection block in Fig. 5 outputs $\boldsymbol{\tau}_{mf}$ and $\boldsymbol{\delta\tau}_f$ at t_{col} to identify the collided cable. A time function $s(t)$, with a 2-second transition, is then defined to avoid sudden reductions in tension. A selector matrix $\mathbf{SI}$ isolates the collided cable:
$$\mathbf{SI} = \mathrm{diag}(\delta_{1,c},\ \delta_{2,c},\ \ldots,\ \delta_{8,c}), \tag{28}$$
where $\delta_{i,j} = 1$ if $i = j$, and 0 otherwise.
- **Gradual Reduction of the Collided Cable Tension:** Once the collided cable is identified, the proposed strategy in [30] reduces the desired cable tension using a tension distribution algorithm, blocks joint correction, and simultaneously increases the length of the collided cable to induce sagging. To ensure effectiveness, closed-loop cable tension tracking is employed. The management function $\mathbf{S}(t)$, obtained via $s(t) \cdot \mathbf{SI}$, decreases $\boldsymbol{\tau}_{\max}$ until reaching the minimum tension $\boldsymbol{\tau}_{\min}$. Concurrently, the cable release is calculated, transitioning the desired joint angle from $\hat{\mathbf{q}}_d$ to $\mathbf{q}_d$ by adding the optimal cable increment δl_c. The axial stiffness (ES) is determined using a cable identification experimental apparatus rather than relying on the manufacturer's value, the errors in estimation would negatively impact the accuracy of the cable release [43].
- **Detection of Collision End:** According to [30], the collision ends if δl_c remains below 0.1 mm for 1 second.
- **Post-Collision Restoration:** After detecting collision termination, $\mathbf{S}(t)$ is updated to gradually restore $\boldsymbol{\tau}_{\max}$ and return the cable length to its nominal value. This ensures a smooth transition back to normal operation, preventing discontinuities that may compromise reliability.

Figure 10 illustrates Cable 2 colliding with the human during dynamic motion in the WFW that allows tension release. Upon collision detection, the desired cable tension is decreased to 1 N before the collision ends, and restoration commences one second later, fully recovering within two seconds. The tension profile indicates effective collision management: throughout the event, the involved cable's tension remains under 5 N, a significant improvement compared to Fig. 6, where tension exceeded 40 N, thereby enhancing operator safety during human–robot interaction. The rapid tension drop causes the cable to sag and reduces its contribution to platform support. Consequently, an observable oscillation of the moving-platform may occur, as the mechanical configuration momentarily resembles a cable-loss scenario with asymmetrical tension distribution. Such transient motions are clearly visible in the supplementary video. While the platform remains stable within the feasible workspace and eventually settles, future implementations could incorporate active damping mechanisms—such as sliding-mode or adaptive control [44]—to attenuate these oscillations and improve post-collision recovery stability.

C. SC3: Human–MP Collision

In real-world human–MP collision scenarios, the robot often lacks prior information regarding the human's position, and visual data may be obscured. Consequently, the contact forces, either measured [17] or estimated using the collision identification algorithms shown in Fig. 5, can be employed to modify the desired trajectory in Cartesian space. Compliance control adjusts the desired trajectory in response to external forces acting on the cable. When a human–MP collision occurs, the general form of the compliance control equation [36] is given by

$$\mathbf{M}_i(\dot{\mathbf{v}}_0 - \dot{\mathbf{v}}_d) + \mathbf{B}_i(\mathbf{v}_0 - \mathbf{v}_d) + \mathbf{K}_i(\mathbf{p}_0 - \mathbf{p}_d) = \mathbf{w}, \tag{29}$$

where $\mathbf{M}_i$ denotes the inertia matrix, $\mathbf{B}_i$ the damping matrix, and $\mathbf{K}_i$ the desired stiffness matrix. The vectors $\mathbf{p}_d$, $\mathbf{v}_d$, and $\dot{\mathbf{v}}_d$ represent the desired position, velocity, and acceleration, respectively, while $\mathbf{p}_0$, $\mathbf{v}_0$, and $\dot{\mathbf{v}}_0$ denote the reference position, velocity, and acceleration. The term $\mathbf{w}$ represents the external wrench acting on the system.

Rearranging (29) to express the acceleration error yields

$$\dot{\mathbf{v}}_0 - \dot{\mathbf{v}}_d = \mathbf{M}_i^{-1}\left[\mathbf{w} - \mathbf{B}_i(\mathbf{v}_0 - \mathbf{v}_d) - \mathbf{K}_i(\mathbf{p}_0 - \mathbf{p}_d)\right]. \tag{30}$$

For a given net force discrepancy, a larger inertia matrix $\mathbf{M}_i$ reduces the magnitude of the acceleration error. However, increasing $\mathbf{M}_i$ also affects the dynamic response by lowering both the natural frequency and the damping ratio [36]. The natural frequency is defined as

$$\boldsymbol{\omega}_n = \sqrt{\frac{\mathbf{K}_i}{\mathbf{M}_i}}, \tag{31}$$

and the damping ratio is defined as

$$\boldsymbol{\zeta} = \frac{\mathbf{B}_i}{2\sqrt{\mathbf{K}_i\mathbf{M}_i}}. \tag{32}$$

This reduction results in a slower transient response. In industrial applications, high-precision acceleration tracking and rapid responsiveness to external forces are essential to move the MP away from the human operator when a collision occurs. Therefore, the adaptive compliant trajectory controller shown in Fig. 9 is employed.

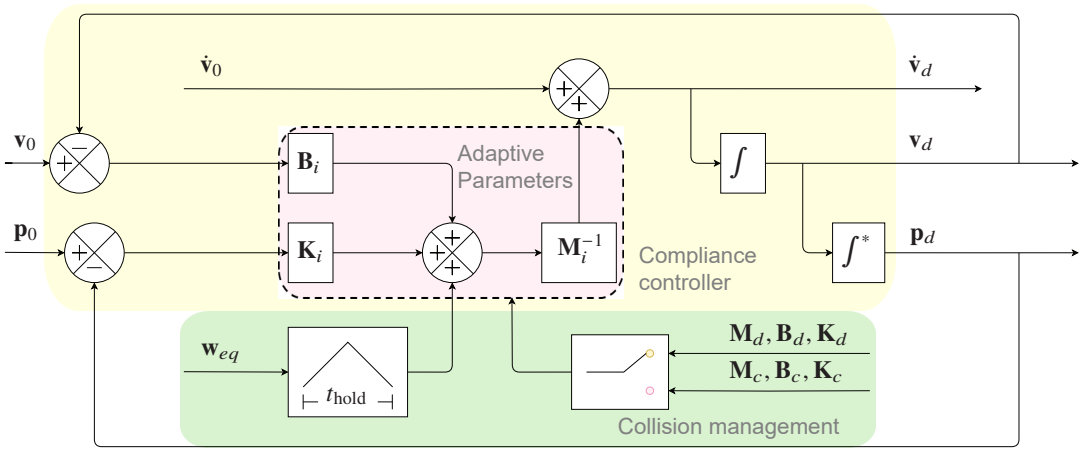

Fig. 9: Schematic of the adaptive compliant trajectory controller (detailed diagram as shown in Fig. 5). The yellow patch indicates the compliance controller operating under nominal conditions when no contact is detected. In the pink patch, the controller employs adaptive parameters based on the current contact scenario. The green patch represents the collision management, which selects the appropriate parameter set and incorporates a triangular buffer for the estimated external wrench $\mathbf{w}_{eq}$ along with the holding time t_{hold} to ensure a smooth transition back to the desired trajectory. Note that $\int$ denotes the integration symbol, and $\int^*$ represents the modified integration symbol that accounts for the rotation matrix.

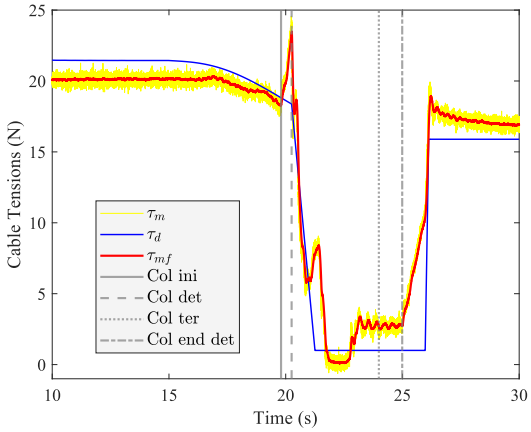

Fig. 10: Evolution of Cable 2 tensions and collision response under human–cable collision management. Here, 'Col' indicates collision, 'ini' indicates initialization, 'det' indicates detection, and 'ter' indicates termination.

In Fig. 9, the yellow patch indicates the compliance controller that is active when no contact is detected. In the pink patch, the compliant trajectory controller uses adaptive parameters depending on the contact scenarios. These parameters include the desired inertia $\mathbf{M}_d$, damping $\mathbf{B}_d$, and stiffness $\mathbf{K}_d$, while an alternative set of parameters, $\mathbf{M}_c$, $\mathbf{B}_c$, and $\mathbf{K}_c$, is applied when contact is detected and classified as a human–MP collision. Accordingly, the following equations are obtained:

$$\mathbf{M}_d(\dot{\mathbf{v}}_0 - \dot{\mathbf{v}}_d) + \mathbf{B}_d(\mathbf{v}_0 - \mathbf{v}_d) + \mathbf{K}_d(\mathbf{p}_0 - \mathbf{p}_d) = 0, \quad (33)$$

$$\mathbf{M}_c(\dot{\mathbf{v}}_0 - \dot{\mathbf{v}}_d) + \mathbf{B}_c(\mathbf{v}_0 - \mathbf{v}_d) + \mathbf{K}_c(\mathbf{p}_0 - \mathbf{p}_d) = \mathbf{w}_{eq}, \quad (34)$$

where $\mathbf{w}_{eq}$ denotes the estimated external wrench acting on the system, obtained from (19). Equations (33) and (34) describe the system behavior for the cases without and with active collision management, respectively. Compared to conventional compliance methods such as the Cartesian-space admittance scheme in [16], [45], the proposed approach extends previous work by introducing an adaptive compliance strategy that modulates stiffness based on real-time contact conditions, without requiring external force sensors. Consequently, the controller maintains high stiffness of the MP during unconstrained motion to preserve precise trajectory tracking, but immediately reduces stiffness upon collision detection, thereby limiting impact forces and ensuring safe, stable interaction in compliance with ISO/TS 15066 force limits. These features make the proposed method more suited to real-world human–robot interaction, where collisions can occur from arbitrary directions.

The management phase terminates when the Cartesian distance between the reference and compliant trajectories remains below 0.01 m for 1 s. Note that purely orientational compliant trajectories are not considered in this study, as they do not enable the MP to move away from the human. However, such cases can be detected through cable tension error analysis, and additional functions can be implemented to address them.

The green patch in Fig. 9 represents the SC3 management for the compliance controller, where the parameter t_{hold} and the corresponding block constitute a triangular buffer for the estimated external wrench $\mathbf{w}_{eq}$. The rationale for this buffer is based on two considerations. First, although the adaptive compliance controller is primarily designed for human–robot collaboration [46], the management strategy employed herein aims to move the MP away from the human to prevent potential subsequent collisions. During compliant control, contact between the human and MP may cease and subsequently resume, thereby necessitating a holding mechanism. Second, when returning to the desired trajectory, the estimation of $\mathbf{w}_{eq}$ may exhibit significant errors; incorporating this noisy signal into (34) can result in inconsistent solutions and impulsive

responses that may exceed the system's control torque capacity or impose an excessive computational load, thereby destabilizing the MP.

In practice, the compliant parameters are selected based on the system properties; notably, the desired inertia $\mathbf{M}_d$ is taken as the measured inertia of the system. Accordingly, the collision inertia matrix is defined as

$$\mathbf{M}_c = \kappa\,\mathbf{M}_d. \tag{35}$$

Here, $\kappa \in (0, 1]$ is a scalar gain that *rescales* the collision-mode impedance: a smaller κ lowers the apparent inertia while proportionally increasing damping and stiffness. Consequently, the natural frequency and damping ratio rise by $1/\kappa$, producing a faster, low-impedance motion that safely drives the MP away from the operator. The damping and stiffness in the collision mode are defined as

$$\mathbf{B}_c = \frac{\mathbf{B}_d}{\kappa}, \quad \mathbf{K}_c = \frac{\mathbf{K}_d}{\kappa}. \tag{36}$$

This configuration increases the natural frequency $\boldsymbol{\omega}_n$ and the damping ratio $\boldsymbol{\zeta}$ relative to their nominal values scaled by $\frac{1}{\kappa}$. The introduction of κ and t_{hold} provides a compromise that enables safe trajectory modification during collision events while preserving overall system stability.

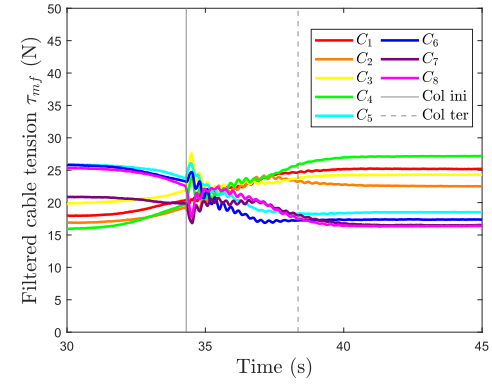

(a) Filtered cable tensions

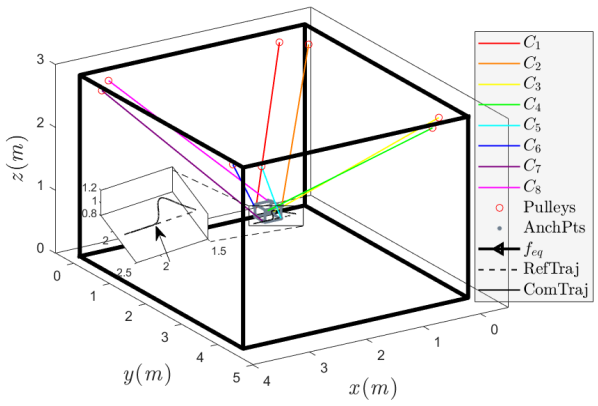

(b) Reference and compliant trajectory

Fig. 11: Filtered cable tensions (top) and comparison of reference with compliant trajectory in space view (bottom).

Figure 11 illustrates the filtered cable tensions and the evolution of the reference trajectory (dashed line) alongside the compliant trajectory (solid black line). Upon detecting a human–MP collision, the MP smoothly adapts its path and eventually returns to the reference trajectory; the parameters $t_{\text{hold}} = 4$ s and $\kappa = 0.1$ ensure a safe deviation. In Fig. 11a, a slight oscillation is observed during the 4 s interval in which $\mathbf{w}_{eq}$ is applied, but the compliant trajectory gradually converges with the reference. The proposed method effectively directs the MP away from the operator by modifying the trajectory and then automatically resumes the nominal path once contact ends.

Future work will focus on optimizing the external wrench estimation and the computational efficiency of the compliance controller. An adaptive compliance controller that relies on real-time estimation is planned. This controller will not only adjust the Cartesian trajectory but also adapt the cable tension distribution to maintain MP stability, thus aligning with research on human–MP collaborative manipulation.

VII. Conclusion

This paper presented a comprehensive framework for detecting, distinguishing, and managing contact events in human-assisted CDPR carrying tasks. The proposed method classifies three frequently encountered interaction scenarios: payload placement and removal, human–cable collisions, and human–MP collisions. Unlike traditional collision detection methods that rely on single force thresholds, our approach employs frequency-domain analysis of the estimated external wrench to compute Spectral Norm Derivative (SND) indices for force and moment components. These indices, coupled with a scoring-based criterion, reliably distinguish contact scenarios in real-time, even under dynamic operating conditions. Experimental results demonstrated that updating the robot's mass estimate upon payload placement significantly improves trajectory tracking, and rapidly releasing tension in the collided cable effectively enhances operator safety. Moreover, the implementation of a compliant controller successfully resolved human–MP collisions, allowing safe deviations and smooth recovery of the robot's trajectory after collision events.

The experimental evaluations underscore the high safety and reliability achieved by the proposed approach, without compromising overall performance and productivity. Nonetheless, several important avenues remain open for future research.

First, while this study currently treats human–cable and human–MP collisions strictly as safety risks, future investigations could reframe such interactions as opportunities for deeper collaboration. Leveraging advanced contact distinction methods, along with refined threshold tuning and adjusted scoring configurations, could enable more nuanced and cooperative responses.

Second, the deterministic scoring-based classifier employed here provides strong interpretability and ensures real-time applicability; however, it lacks the probabilistic output capabilities of soft classification models. Integrating probabilistic approaches, such as softmax activation functions or Bayesian decision layers, would enable graded responses and improved

uncertainty quantification. Yet, the implementation of these models demands additional parameters and substantially more training data, which are currently restricted due to the safety and ethical constraints surrounding human–robot collision experiments.

Third, expanding the diversity of experimental conditions and participant profiles is critical for further validating and generalizing the method. Future experiments involving more participants, varied collision types, and realistic industrial scenarios will require formal ethical approvals and strengthened safety protocols. Data obtained from these expanded experiments could then be leveraged to enhance transparency and confirm the robustness and safety of human–robot collaborative systems [47]. Physics-informed neural networks (PINNs) represent a promising avenue for incorporating physical and dynamic modeling directly into contact classification frameworks, potentially reducing dependence on purely empirical data. Currently, the limited number of physical trials available restricts effective training of such complex models. One solution is the generation of synthetic datasets through validated multi-physics simulators capable of safely replicating diverse contact dynamics. This simulation-based methodology could significantly accelerate future deployment of PINNs and probabilistic classifiers, circumventing experimental limitations.

Fourth, the present tension-based detector cannot sense near-contact or purely proximity interactions. One possible extension would be to add capacitive sensing [48] along the cables [49]. In theory, the small capacitance variations produced by an approaching human could be analysed with a modified version of the current SND pipeline, but this would require additional filtering and a careful frequency-band selection that has not yet been validated. We therefore regard capacitive sensing as a promising topic for future work rather than a ready-to-deploy solution.

Finally, the assumption that warrants further exploration involves releasing cable tension in the WFW. When a cable collision occurs, the current method assumes that the collided cable can be safely released within its feasible range. Future studies will incorporate a trajectory-compliant controller that repositions the MP into a region of the workspace where cable release is possible if it is not initially feasible. This enhancement would bolster the versatility of the proposed architecture, making it applicable to a wider variety of industrial and logistical tasks.

ACKNOWLEDGMENT

The first author is funded by the China Scholarship Council (Grant No. 202208070012). The authors gratefully acknowledge the assistance of Dr. Marceau Métillon during the experiments, and thank M. Étienne Delemazure for his mechanical engineering support, including the manufacturing and installation of experimental components. The authors also wish to thank Dr. Arda Yiğit and Dr. Rıdvan Keskin for their valuable comments and constructive feedback. The authors would also like to thank Prof. Yannick Aoustin for insightful discussions. ChatGPT was used solely for grammar checking and language polishing purposes.

REFERENCES

[1] S. Briot and W. Khalil, *Dynamics of parallel robots: From rigid bodies to flexible elements*. Springer, 2015, vol. 35.

[2] Z. Zake, F. Chaumette, N. Pedemonte, and S. Caro, "Vision-based control and stability analysis of a cable-driven parallel robot," *IEEE Robotics and Automation Letters*, vol. 4, pp. 1029–1036, 2019.

[3] Z. Zhang, Z. Shao, L. Wang, and A. J. Shih, "Optimal design of a high-speed pick-and-place cable-driven parallel robot," in *Cable-driven parallel robots: proceedings of the third international conference on cable-driven parallel robots*. Springer, 2018, pp. 340–352.

[4] A. Lucarini, E. Idà, and M. Carricato, "Optimal design of a deployable and reconfigurable cable-driven parallel robot," in *2024 20th IEEE/ASME International Conference on Mechatronic and Embedded Systems and Applications (MESA)*, 2024, pp. 1–6.

[5] M. Khadem, F. Inel, G. Carbone, and A. S. T. Tich, "Experiment and validation of open-loop control on the simulation of a cable-driven planar robot for drawing and writing tasks," *Archives of Advanced Engineering Science*, 2023.

[6] J.-B. Izard, A. Dubor, P.-E. Hervé, E. Cabay, D. Culla, M. Rodriguez, and M. Barrado, "Large-scale 3d printing with cable-driven parallel robots," *Construction Robotics*, vol. 1, pp. 69–76, 2017.

[7] I. Ben Hamida, M. A. Laribi, A. Mlika, L. Romdhane, S. Zeghloul, and G. Carbone, "Multi-objective optimal design of a cable driven parallel robot for rehabilitation tasks," *Mechanism and Machine Theory*, vol. 156, p. 104141, 2021.

[8] M. Duan, J. Feng, and S. Liu, "Design, manufacturing, modelling, and control of a cable-driven parallel robot for additive manufacturing," in *2023 IEEE 19th International Conference on Automation Science and Engineering (CASE)*, 2023, pp. 1–6.

[9] T. Rousseau, C. Chevallereau, and S. Caro, "Human-cable collision detection with a cable-driven parallel robot," *Mechatronics*, vol. 86, p. 102850, 2022.

[10] A. Weiss, A.-K. Wortmeier, and B. Kubicek, "Cobots in industry 4.0: A roadmap for future practice studies on human–robot collaboration," *IEEE Transactions on Human-Machine Systems*, vol. 51, no. 4, pp. 335–345, 2021.

[11] D. Rodriguez-Guerra, G. Sorrosal, I. Cabanes, and C. Calleja, "Human-robot interaction review: Challenges and solutions for modern industrial environments," *Ieee Access*, vol. 9, pp. 108 557–108 578, 2021.

[12] A. Hanna, S. Larsson, P.-L. Götvall, and K. Bengtsson, "Deliberative safety for industrial intelligent human–robot collaboration: Regulatory challenges and solutions for taking the next step towards industry 4.0," *Robotics and Computer-Integrated Manufacturing*, vol. 78, p. 102386, 2022.

[13] A. Cherubini, R. Passama, A. Crosnier, A. Lasnier, and P. Fraisse, "Collaborative manufacturing with physical human–robot interaction," *Robotics and Computer-Integrated Manufacturing*, vol. 40, pp. 1–13, 2016.

[14] A. Mohammad, M. Schappler, and T. Ortmaier, "Towards human-robot collaboration with parallel robots by kinetostatic analysis, impedance control and contact detection," in *2023 IEEE International Conference on Robotics and Automation (ICRA)*. IEEE, 2023, pp. 12 092–12 098.

[15] P. Tsarouchi, S. Makris, and G. Chryssolouris, "Human–robot interaction review and challenges on task planning and programming," *International Journal of Computer Integrated Manufacturing*, vol. 29, no. 8, pp. 916–931, 2016.

[16] M. Métillon, C. Charron, K. Subrin, and S. Caro, "Stiffness and transparency of a collaborative cable-driven parallel robot," in *International Symposium on Advances in Robot Kinematics*. Springer, 2022, pp. 101–109.

[17] ——, "Performance and interaction quality variations of a collaborative cable-driven parallel robot," *Mechatronics*, vol. 86, p. 102839, 2022.

[18] A. Mohammad, T.-L. Habich, T. Seel, and M. Schappler, "Safepr: Unified approach for safe parallel robots by contact detection and reaction with redundancy resolution," *arXiv preprint arXiv:2501.17773*, 2025.

[19] "ISO/TS 15066:2016 robots and robotic devices – collaborative robots," https://www.iso.org/standard/62996.html, 2016, international Organization for Standardization.

[20] L. Blanchet and J.-P. Merlet, "Interference detection for cable-driven parallel robots (cdprs)," in *2014 IEEE/ASME International Conference on Advanced Intelligent Mechatronics*. IEEE, 2014, pp. 1413–1418.

[21] R. Meziane, P. Cardou, and M. J.-D. Otis, "Cable interference control in physical interaction for cable-driven parallel mechanisms," *Mechanism and Machine Theory*, vol. 132, pp. 30–47, 2019.

[22] S. Caro and J.-P. Merlet, "Failure analysis of a collaborative 4-1 cable-driven parallel robot," in *New Trends in Mechanism and Machine Science: EuCoMeS 8*. Springer, 2020, pp. 440–447.
[23] G. Boschetti and R. Minto, "A sensorless approach for cable failure detection and identification in cable-driven parallel robots," *Robotics and Autonomous Systems*, vol. 183, p. 104855, 2025.
[24] X. Chang, T. Liu, S. Jiao, and Z. Yang, "Rrt*-apf hybrid path planning for reconfigurable cable-driven parallel robots," in *2024 9th International Conference on Automation, Control and Robotics Engineering (CACRE)*. IEEE, 2024, pp. 413–420.
[25] E. Khoshbin, M. J.-D. Otis, and R. Meziane, "Reconfigurable cable-driven parallel mechanism design: physical constraints and control," *Robotica*, pp. 1–47, 2024.
[26] H. An, D. Yu, W. Xu, and H. Yuan, "Modeling and cooperation method for movable anchor winch cable-driven parallel robot," *IEEE/ASME Transactions on Mechatronics*, 2024.
[27] G. Xu, H. Zhu, H. Xiong, and Y. Lou, "Data-driven dynamics modeling and control strategy for a planar n-dof cable-driven parallel robot driven by n+ 1 cables allowing collisions," *Journal of Mechanisms and Robotics*, vol. 16, no. 5, 2024.
[28] H. Xiong, Y. Xu, Y. Yu, and Y. Lou, "Cable path analysis and kinematic control of a cable-driven parallel robot allowing cables to wrap on cylinders or spheres," *Journal of Mechanisms and Robotics*, vol. 17, no. 1, 2025.
[29] H. Gao, C. Chevallereau, and S. Caro, "Detection and Management of Human-Cable Collision in Cable-Driven Parallel Robots," *IEEE Robotics and Automation Letters*, vol. 9, no. 12, pp. 11 698–11 705, Dec. 2024. [Online]. Available: https://hal.science/hal-04851656
[30] ——, "Advancements in human-cable collision detection and management in cable-driven parallel robots," in *Proceedings of the Seventh International Conference on Cable-Driven Parallel Robots*, Hong Kong, China, Jul 2025. [Online]. Available: https://hal.science/hal-04912207
[31] J. Garrido, D. Silva-Muñiz, E. Riveiro, J. Rivera-Andrade, and J. Sáez, "Collaborative behavior for non-conventional custom-made robotics: a cable-driven parallel robot application," *Machines*, vol. 12, no. 2, p. 91, 2024.
[32] G. Cortigiani, M. Malvezzi, D. Prattichizzo, and M. Pozzi, "Human-robot collaborative cable-suspended manipulation with contact distinction," *IEEE Robotics and Automation Letters*, vol. 10, no. 1, pp. 740–747, 2025.
[33] S. Golz, C. Osendorfer, and S. Haddadin, "Using tactile sensation for learning contact knowledge: Discriminate collision from physical interaction," in *2015 IEEE International Conference on Robotics and Automation (ICRA)*. IEEE, 2015, pp. 3788–3794.
[34] C.-N. Cho, J.-H. Kim, Y.-L. Kim, J.-B. Song, and J.-H. Kyung, "Collision detection algorithm to distinguish between intended contact and unexpected collision," *Advanced Robotics*, vol. 26, no. 16, pp. 1825–1840, 2012.
[35] F. Franzel, T. Eiband, and D. Lee, "Detection of collaboration and collision events during contact task execution," in *2020 IEEE-RAS 20th International Conference on Humanoid Robots (Humanoids)*. IEEE, 2021, pp. 376–383.
[36] A. Kouris, F. Dimeas, and N. Aspragathos, "Contact distinction in human-robot cooperation with admittance control," in *2016 IEEE International Conference on Systems, Man, and Cybernetics (SMC)*. IEEE, 2016, pp. 001 951–001 956.
[37] ——, "A frequency domain approach for contact type distinction in human–robot collaboration," *IEEE robotics and automation letters*, vol. 3, no. 2, pp. 720–727, 2018.
[38] R. Dhakate, T. Jantos, E. Allak, S. Weiss, and J. Steinbrener, "Carosac: A reinforcement learning-based kinematic control of cable-driven parallel robots by addressing cable sag through simulation," *IEEE Robotics and Automation Letters*, 2025.
[39] Y. Sugahara, G. Chen, N. Atsumi, D. Matsuura, Y. Takeda, R. Mizutani, and R. Katamura, "A suspended cable-driven parallel robot for human-cooperative object transportation," in *ROMANSY 23-Robot Design, Dynamics and Control: Proceedings of the 23rd CISM IFToMM Symposium 23*. Springer, 2021, pp. 109–117.
[40] S. Baklouti, S. Caro, and E. Courteille, "Sensitivity analysis of the elasto-geometrical model of cable-driven parallel robots," in *Cable-Driven Parallel Robots: Proceedings of the Third International Conference on Cable-Driven Parallel Robots*. Springer, 2018, pp. 37–49.
[41] S. Baklouti, E. Courteille, S. Caro, and M. Dkhil, "Dynamic and oscillatory motions of cable-driven parallel robots based on a nonlinear cable tension model," *Journal of mechanisms and robotics*, vol. 9, no. 6, p. 061014, 2017.
[42] L. Gagliardini, M. Gouttefarde, and S. Caro, "Determination of a dynamic feasible workspace for cable-driven parallel robots," *Advances in Robot Kinematics 2016*, pp. 361–370, 2018.
[43] S. Nanthacoumarane, B. Wang, A. Kouadri-Henni, P. Cardou, and S. Caro, "Polymer Cable Characterization in Cable-Driven Parallel Robots," in *25ème Congrès Français de Mécanique Nantes*, Nantes, France, Aug. 2022. [Online]. Available: https://hal.science/hal-03758221
[44] V. Di Paola, S. Caro, and M. Zoppi, "Design and performance investigation of a sliding-mode adaptive proportional–integral–derivative control for cable-breakage scenario," *Meccanica*, pp. 1–11, 2024.
[45] J. Jun, X. Jin, A. Pott, S. Park, J.-O. Park, and S. Y. Ko, "Hybrid position/force control using an admittance control scheme in cartesian space for a 3-dof planar cable-driven parallel robot," *International Journal of Control, Automation and Systems*, vol. 14, no. 4, pp. 1106–1113, 2016.
[46] S. Haddadin and E. Croft, "Physical human–robot interaction," *Springer handbook of robotics*, pp. 1835–1874, 2016.
[47] J. L. Wright, J. Y. Chen, and S. G. Lakhmani, "Agent transparency and reliability in human–robot interaction: The influence on user confidence and perceived reliability," *IEEE Transactions on Human-Machine Systems*, vol. 50, no. 3, pp. 254–263, 2019.
[48] L. K. Baxter, *Capacitive Sensors: Design and Applications*. Wiley and IEEE Press, 1997.
[49] M. Métillon, L. Rasolofondraibe, R. Gayol, L. Contal, S. Acoulon, C. Charron, K. Subrin, and S. Caro, "A capacitive cable-based detection device for cable-driven parallel robots," Poster presented at CableCon 2023, 2023. [Online]. Available: https://cablecon2023.sciencesconf.org/resource/page/id/17

Hanbang Gao received his master's degree from École Centrale de Nantes, Nantes, France, in 2022. He is currently a Ph.D. candidate in Mechanics and Robotics at École Centrale de Nantes. He is a member of the RoMaS (Robots and Machines for Manufacturing, Society, and Services) and REV (Robotique et Vivant) teams at LS2N (Laboratoire des Sciences du Numérique de Nantes). His research focuses on safety in physical human-robot interaction and human-robot collaboration in Cable-Driven Parallel Robots.

Christine Chevallereau received the master's and Ph.D. degrees from École Nationale Supérieure de Mécanique, Nantes, France, in 1985 and 1988, respectively. Since 1989, she has been with the CNRS, Institut de Recherche en Communications et Cybernétique de Nantes, and Laboratoire des Sciences du Numérique de Nantes (LS2N), École Centrale de Nantes, where she was the deputy director between 2017 and 2021. She is also the head of the REV (Robotique Et Vivant) team, which conducts research in robotics at the interface with living systems. In 2025, she was awarded the CNRS Silver Medal (**Médaille d'argent du CNRS**). Her research interests include modeling and control of manipulators and locomotor robots, in particular biped, bio-inspired robot and robot driven by cables.

Stéphane Caro received his Engineering and M.Sc. degrees in mechanical engineering from École Centrale Nantes in 2001, and his Ph.D. in mechanical engineering from the University of Nantes in 2004. He was a Post-doctoral Fellow in the Centre for Intelligent Machines, McGill University, Montreal, Canada from 2005 to 2006. He is currently CNRS Research Director, the head of the Robots and Machines for Manufacturing Society and Services (RoMaS) Team at LS2N and a part-time researcher at IRT Jules Verne. His research interests include design, modelling and control of cable-driven parallel robots and reconfigurable parallel robots.